

Mechanically Stable, Binder-Free, and Free-Standing Vanadium Trioxide/Carbon Hybrid Fiber Electrodes for Lithium-Ion Batteries

Behnoosh Bornamehr, Markus Gallei, Samantha Husmann, and Volker Presser*

Binder is a crucial component in present-day battery electrodes but commonly contains fluorine and requires coating processing using organic (often toxic) solvents. Preparing binder-free electrodes is an attractive strategy to make battery electrode production and its end-of-use waste greener and safer. Herein, electrospinning is employed to prepare binder-free and self-standing electrodes. Such electrodes often suffer from low flexibility, and the correlation between performance and flexibility is usually overlooked. Processing parameters affect the mechanical properties of the electrodes, and for the first time it is reported that mechanical flexibility directly influences the electrochemical performance of the electrode. The importance is highlighted when processing parameters advantageous to powder materials, such as a higher heat treatment temperature, harm self-standing electrodes due to deterioration of fiber flexibility. Other strategies, such as conductive carbon addition, can be employed to improve the cell performance, but their effect on the mechanical properties of the electrodes must be considered. Rapid heat treatment achieves self-standing V_2O_3 with a capacity of 250 mAh g^{-1} at 250 mA g^{-1} and 390 mAh g^{-1} at 10 mA g^{-1}

synthesized material by electrospinning has an open and porous structure with a high surface area which can be used in different applications, such as filtering and purification,^[3] as drug carrier mesh in drug delivery,^[4,5] or serving as a template for producing inorganic nanofibers in composites.^[6] An application of the electrospun fibers that is gaining more importance is energy storage and conversion, specifically secondary battery electrodes, due to their simple and versatile synthesis and the ability to modify the surface with conductive coatings or by nanostructuring to improve the capacity and charge transfer.^[7,8]

Electrospun fibers are attractive as they form continuous fibrous morphology, are versatile in transforming a variety of polymers and inorganic substances into nanostructured materials, and can be used to avoid the use of binders to produce self-standing binder-free electrodes.^[9] Binders

1. Introduction

Electrospinning is a facile synthesis method to produce fibers with a diameter of tens of nanometers to micrometers.^[1,2] The

B. Bornamehr, S. Husmann, V. Presser
INM – Leibniz Institute for New Materials
D2 2, 66123 Saarbrücken, Germany
E-mail: presser@presser-group.com

B. Bornamehr, V. Presser
Department of Materials Science & Engineering
Saarland University
Campus D2 2, 66123 Saarbrücken, Germany

M. Gallei, V. Presser
Saarene – Saarland Center for Energy Materials and Sustainability
66123 Saarbrücken, Germany

M. Gallei
Polymer Chemistry
Saarland University
Campus D4 2, 66123 Saarbrücken, Germany

 The ORCID identification number(s) for the author(s) of this article can be found under <https://doi.org/10.1002/adsu.202200373>.

© 2022 The Authors. Advanced Sustainable Systems published by Wiley-VCH GmbH. This is an open access article under the terms of the Creative Commons Attribution License, which permits use, distribution and reproduction in any medium, provided the original work is properly cited.

DOI: [10.1002/adsu.202200373](https://doi.org/10.1002/adsu.202200373)

are usually high-cost and halogen-containing components in the battery electrode that do not contribute to the capacity and decrease conductivity at their interface with the active material. Accordingly, research has been dedicated to removing binders in the electrode or their substitution by a conductive binder.^[10,11] In addition, electrode processing usually consists of coating slurries composed of the active material, binder, and carbon additive mixed in a solvent, typically highly toxic *N*-methyl-2-pyrrolidone (NMP). Electrospinning can maintain the integrity of the active electrode material without using binders while avoiding the coating process and, thus, using NMP.

Compared to binder-free electrodes synthesized on a substrate such as carbon cloth, carbon nanotubes (CNTs), or other conductive substrates,^[12,13] self-standing electrospun fibers do not have a substrate to give them additional support, and they rely on their mechanical stability.^[14–16] These electrodes can also be a candidate for use in flexible or wearable energy storage devices.^[12] Among materials synthesized by electrospinning for energy storage, vanadium oxides are an attractive candidate due to their various oxide phases, such as VO_2 , V_2O_3 , V_2O_5 , V_3O_7 , and vanadium's multiple oxidation states that give versatility in the design and utilized potential windows for energy storage and conversion.^[17,18] Although electrospinning has great potential as a green synthesis method due to avoiding the use of a binder and one-pot synthesis method without producing

side wastes, often studies on the electrospun fibers do not use these fibers directly as self-standing mats and prepare the electrodes by grinding the fibers and coating them on a substrate. In contrast, electrospun fiber mats offers the possibility of better functional material coverage due to the connected pathways.^[19–21] Although it is known that the mechanical properties of electrospun fibers are correlated with their performance,^[22,23] no report is available on the effect of processing parameters on the mechanical properties and application performance.^[24,25] As a result, although self-standing electrodes are investigated, they are mainly treated similarly to powder-based electrodes, which has imposed a gap in knowledge for the parameters that affect electrochemical performance. Our goal is, therefore, to provide a better understanding of the binder-free, electrospun electrodes.

Here we demonstrate that processing parameters such as heat-treatment temperature, atmosphere, and cooling rate interplay with the mechanical stability of the vanadium oxide electrospun fibers as a self-standing electrode. We also show the beneficial impact of adding conductive carbon to the fibers and the challenges faced in this procedure. By developing electrochemical energy storage materials and applications, our work contributes toward the United Nation's Sustainable Development Goal (SDG) number 7 (Affordable and Clean Energy).

2. Experimental Section

2.1. Synthesis of Electrospun Fibers

Vanadium(V) oxytripropoxide (VITP, 98% metal basis), acetic anhydride (Ac₂O, ≥98% purity), and ethanol (EtOH, analytical standard) were purchased from Sigma-Aldrich. Poly(vinyl acetate) (PVAc, $M_w = 86\,000\text{ g mol}^{-1}$) was purchased from Synthomer. Carbon black was purchased from Nanografi (C-nergy super C65 conductive carbon black). The electrospinning solution was prepared in an MBraun glovebox through sol-gel synthesis according to a previous method with slight modification.^[18] The sol-gel was prepared by mixing 1.93 mL (vanadium triisopropoxy oxide) VTIP, 2.53 mL EtOH, 0.8 mL Ac₂O, and 0.72 g PVAc; this mixture was then stirred for 18 h. For the carbon-containing sample, 100 mg of commercial carbon black (C-nergy super C65) was directly added to the mixture with the other reactants. Samples containing carbon black (CB) were denoted with CB- prefix to the sample name. The solution was viscous and homogeneous the next day and was extracted via a 5 mL syringe to perform electrospinning.

Electrospinning was carried out in an NF-103 V MECC nanofiber system. A blunt tip 21-gauge needle was used to spin the fibers. The humidity and temperature of the electrospinning chamber were set below 20% and between 25 and 30 °C, respectively. The solution was electrospun from a 20 cm height onto an aluminum foil substrate under a potential difference of 28 kV via 1 mL h⁻¹ feeding rate and 1 min intervals for cleaning the needle. The electrospun mat was then put in a climate chamber set to 20 °C and 40% humidity to cross-link for 48 h. Discs of the cross-linked electrospun fiber were punched into 12 mm diameter circles and heat-treated with different treatment parameters.

2.2. Heat-Treatment of Electrospun Fibers

All samples were heat-treated in an inert atmosphere under the Ar gas flow with a 100 cm³ min⁻¹ flow rate. The samples were either heat-treated in a tubular furnace (Carbolite Gero) and denoted with H-prefix, or heat-treated in an infrared furnace (Behr infrared furnace IRF 10) and denoted with IR-prefix to their name. Before any heat treatment, the samples were placed in the middle of the furnace and purged with Ar (99.999%), depending on the size of the quartz tube, for 30 and 60 min for the infrared and tubular furnace, respectively. **Table 1** shows the utilized heat treatments for the electrospun discs and the resulting disc diameter after the heat treatment. The cooling in the infrared furnace was done in multiple steps to reduce thermal stress. All the treatments had a holding time of 30 min. The overall heat-treatment duration, including the Ar-purging, heating, and cooling, was 24 h for the tubular furnace and 2 h for the infrared furnace. To assess the reproducibility of the synthesis, the mean disc diameter after the treatment was measured with a caliper by measuring the diameter of 10 discs from each batch. All samples showed a diameter between 9.5 and 10.5 mm equal to ≈20% diameter reduction during the heat treatment.

2.3. Material Characterization

To characterize the structure morphology and elemental analysis, scanning electron microscopy (SEM) and energy-dispersive X-ray spectroscopy (EDX) were performed using a ZEISS GEMINI 500 microscope coupled with an Xmax detector from Oxford instruments. An acceleration voltage of 1 kV for imaging and 15 kV for spectroscopy was utilized. Sample preparation was done by mounting on double-sided sticky copper tape fixed on an aluminum stub without conductive sputter coating. For elemental analysis, at least 20 points were chosen from random locations from fibers on focus, and the average was calculated.

In addition, transmission electron microscopy (TEM) employed a 2100F system (JEOL) at 200 kV. To prepare the samples, a copper grid coated with lacey carbon was used as the substrate, and the fibers were dispersed in ethanol for 5 min in an ultrasound bath and then dried on the copper grid by dropwise addition.

A D8 Discover diffractometer (BRUKER AXS) with a copper source (Cu K_α, 40 kV, 40 mA), a Göbel mirror, and a 1 mm point focus were used for X-ray diffraction and phase analysis. A 2D VANTEC detector was used. Moreover, an angular range of 20° 2θ was used for 1000 s and repeated 3 times to cover a

Table 1. Heat treatment conditions to prepare the vanadium oxide fibers.

	Heating rate [°C min ⁻¹]	Holding temperature [°C]	Average cooling rate [°C min ⁻¹]
H-400	5	400	Furnace cooling
IRF-400	25	400	5.5
CB-IRF-400	25	400	5.5
IRF-700	45	700	9
CB-IRF-700	45	700	9

For all samples: Argon flow of 100 sccm in all steps.

full range of 10–80° 2θ range. The scans were integrated and normalized to (0100).

We used a Renishaw inVia Raman microscope with an Nd-YAG laser and 633 nm excitation wavelength. Spectrometer calibration was done using a silicon standard. The sample was exposed to a power of 87 μW at the focal point with a numeric aperture of 0.75. For each sample, 10 random points under focus were chosen, and the spectra were recorded with a spectral resolution of 1 cm⁻¹ by applying the laser for 20 s and accumulating 5 spectra. All spectra were stripped from cosmic rays and then normalized to (0100).

Thermogravimetric analysis (TGA) was done by a Netzsch TG-209-1 Libra. The mass changes to 700 °C were recorded under a heating rate of 5 °C min⁻¹ in an oxidative (synthetic air) atmosphere with Ar as protective gas.

2.4. Mechanical Testing

Bending tests were performed by a custom-made instrument consisting of a motorized stage with a minimum step size of 6 nm (Q-545.240, PI) for displacement control and two goniometers for alignment correction. Disc samples with a mass of 2–3 mg and a diameter of 9.5–10.5 mm were vertically fixed on a glass sheet with all-purpose glue for the least inference in the testing. In situ observation was done via a tubular optic (12X UltraZoom, Navitar Inc.) and a camera (DMK 33UX252, ImagingSource). For the bending tests, the vertically standing sample was brought to contact with a flat punch connecting to the force sensor (KD45-2 N, ME-Messsysteme) until reaching a maximum displacement of half of the sample diameter. A loading and unloading velocity of 1 and 0.5 mm s⁻¹ were used for moving the flat punch.

2.5. Electrochemical Characterization

Half-cells were assembled by using CR2032 coin cells. Heat-treated discs were directly used as self-standing electrodes to

assemble cells without further punching or coating and used as the working electrode against lithium chip (11 mm) as counter and reference electrode. Whatman GF/F glass fiber and Celgard 2325 punched into 18 mm diameter discs were used as a separator, and 1 mol L⁻¹ LiPF₆ salt in a mixture of ethylene carbonate and dimethyl carbonate (EC:DMC, 1:1 by volume, BASF SelectiLyte) as the electrolyte. A BioLogic VMP300 potentiostat/galvanostat for cyclic voltammetry within a potential window of 0.01–3.5 V versus Li/Li⁺ at a scan rate of 0.05 mV s⁻¹ was used. An Arbin Battery Cycler was employed to run galvanostatic charge/discharge with potential limitation measurements in the potential range of 0.01–3.5 V versus Li/Li⁺ to test the rate capability and cycling stability at a rate of 250 mA g⁻¹. The electrode mass was, on average, 2.03 ± 0.77 mg for all 23 samples: The mass of each electrode was determined individually and used to normalize the electrochemical performance of each electrode. All electrochemical tests were done in a climate chamber held at 25 ± 1 °C to eliminate the effect of temperature fluctuations.

3. Results and Discussion

3.1. Synthesis of Metal Alkoxide Fibers

Figure 1 schematically shows the synthesis and processing steps. After the sol–gel preparation with or without carbon additive, flexible fibers were spun. These fibers are then directly heated and used as electrodes without further use of solvents or polymers. Therefore, it replaces the binder polyvinylidene fluoride (PVDF) in battery electrodes with PVA, which is a water-soluble and biodegradable polymer, and replaces all organic solvents used in synthesis or coating with ethanol which is one of the greenest solvents for synthesis due to its renewable generation, low persistence in the environment and low toxicity.^[26] After heat treatment under different parameters, such as different atmospheres, temperatures, and heating rates, the samples were cyclically bent and tested as cathodes versus Li metal. The parent

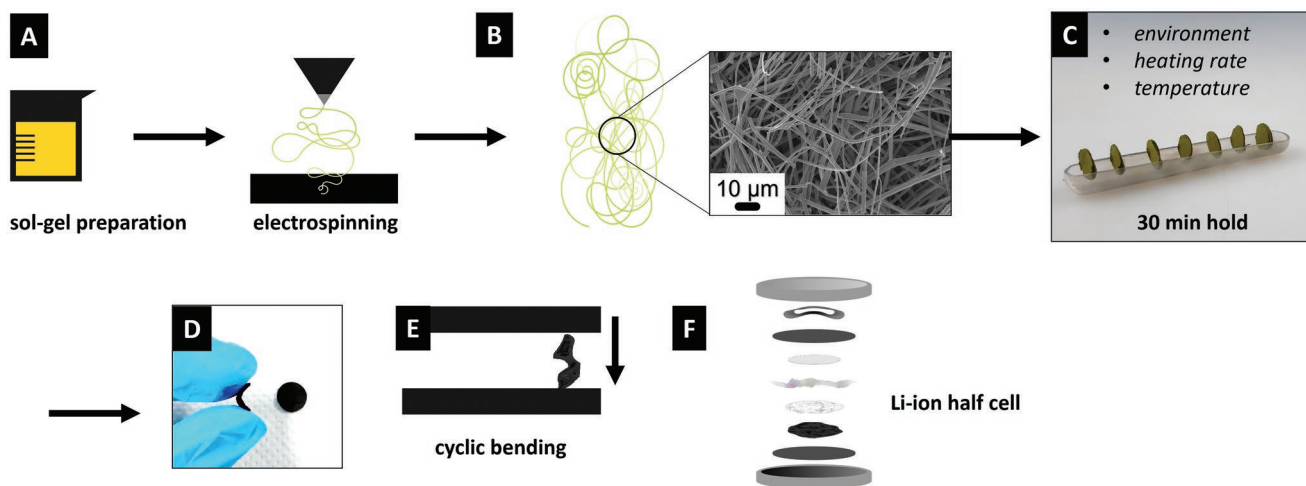


Figure 1. Synthesis and processing procedure to A) prepare a sol–gel as the electrospinning feed and B) electrospun homogeneous fibrous mat, C) punched 12 mm discs from to mat to perform heat-treatments at different conditions with 30 min holding time to D) produce flexible electrodes and be used for E) cyclic bending and F) Li-ion battery electrode.

fibers were prepared from an oxygen-containing vanadium precursor (VTIP) and polymer (PVA) in ethanol. The use of ethanol resulted in a homogeneous fiber morphology without forming beads or droplets due to its quick evaporation.^[27] No additional solvent was used for the fibers with conductive carbon, and the carbon additive was directly added to the solution.

Subsequently, the fibers were treated under different heat-treatment procedures in an infrared furnace at 400 °C for 30 min to form vanadium oxide (VO_x). The effect of the environment was tested as the first parameter affecting the fiber morphology and properties. For this, self-standing as-spun fibers were heat treated in an oxidative environment with a gas flow of 50:50 sccm, Ar/synthetic air, and 100:10 sccm Ar/synthetic air and in an inert environment with Ar only present. At the flow of 50:50 sccm Ar/synthetic air pure crystalline V₂O₅ was achieved (Figure S1A, Supporting Information). This showed similar rod-shaped-vanadium pentoxide nanowires (Figure 2A,B), as reported by Mai et al.^[20] No residual fiber morphology was observed in scanning electron micrographs, and the product showed no mechanical stability and was pulverized upon touch. Better mechanical stability was observed using 100:10 sccm Ar/synthetic air.

Scanning electron characterization showed the fibrous morphology is preserved while large particles are grown from the fibers (Figure 2C,D). X-ray diffraction (XRD) confirmed the present phase is crystalline VO₂ (Figure S1B, Supporting Information). The most homogeneous morphology was achieved under an inert atmosphere (Figure 2E,F). Fibers fully retained their shape while transforming into crystalline V₂O₃, confirmed by XRD and TEM (Figures S1C and S2A,B, Supporting Information). Only the V₂O₃ fibers were self-standing among the samples in different environments. The polymer burning accompanied by the higher oxygen-to-vanadium ratio, led to a disintegration of the fibers, coarsening of VO_x particles, and high brittleness. Therefore, the effect of other processing parameters was investigated using an inert atmosphere, and the oxygen atoms in the VTIP functioned as the oxidation source to form VO_x. A minimum temperature of 400 °C was needed to provide the required energy for achieving crystalline homogeneous vanadium oxide. We observed that the brittleness of the fibers accompanied the formation of VO₂ and V₂O₅ even under short heat treatments. Only the controlled formation of V₂O₃ resulted in a self-standing and flexible electrode with a lower oxygen ratio. This is in line with the reports on self-standing,

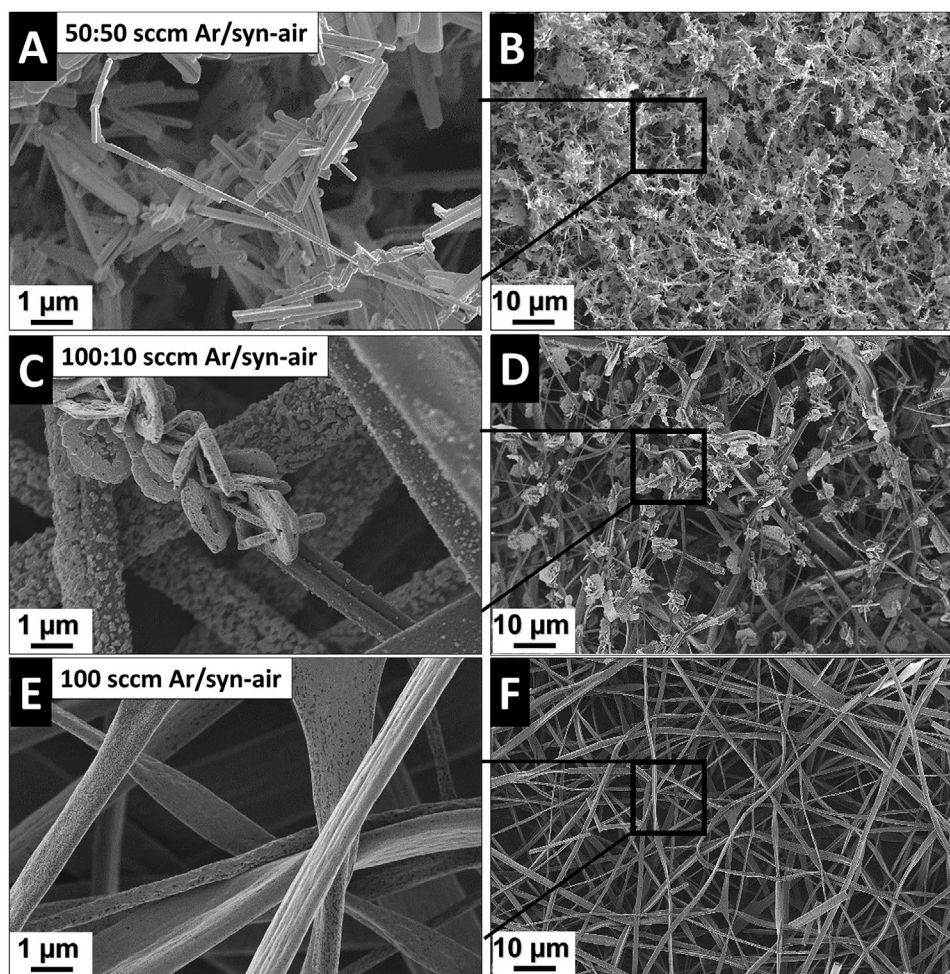


Figure 2. Scanning electron micrographs of heat-treated as-spun fibers for 30 min at 400 °C under A,B) Ar, syn-air/50:50 sccm, C,D) Ar, syn-air/100:10 sccm IRF-700, E,F) Ar/100 sccm.

flexible V_2O_3 , while studies on electrospun fibers of other vanadium oxides do not report flexibility.^[18,20,21,24]

3.2. Heat Treatment of Fibers

After atmosphere optimization for achieving self-standing electrodes, the effect of temperature and heating rate was tested on the properties of the V_2O_3 fibers. For this, the initial heat treatment under Ar was heated to 400 °C in a 1000 s ramp and held for 30 min (IRF-400). The cooling was optimized in multiple steps to minimize the deformation in the samples, as seen by the bending and distortion of the electrospun discs. For this, the cooling from 400 to 50 °C was done in 4 steps of 400–300, 300–200, 200–100, and 100–50 °C. Every step was done with a cooling ramp of 1000 s. The temperatures were optimized to increase the mechanical stability and minimize the deformation caused by the thermal stress in the samples. It was visually observed that the samples were more sensitive to fast cooling than fast heating and showed more deformation during the cooling. Therefore, the cooling was carried out in a step-wise manner. Samples were also heat-treated with multistep heating, but no effect on deformation was observed by changing the heating rate. This means the effect of processing parameters is more pronounced by the thermal contraction of the solid V_2O_3 fibers than when the metal alkoxide is transformed into vanadium oxide. Therefore, the heating was done in a single step, and the cooling was done in multiple steps to achieve flat V_2O_3 discs with the least distortion.

Heat treatments at higher temperatures were also done to achieve a higher crystallinity in the sample and evaluate the effect of the treatment temperature on the electrochemical performance. The heat treatment was optimized to 700 °C for

30 min. Like the IRF-400, the heating was done in a 1000 s ramp from room temperature to 700 °C and held for 30 min. The cooling was done in 4 steps: 700–400, 400–300, 300–200, and 200–100 °C, and each cooling step was done in 1000 s. No control over the temperature was done from 100 °C to RT. Therefore, both heat treatments for IRF-400 and IRF-700 resulted in a 1:36 h duration. The heat-treatments in the infrared furnace were also performed on the carbon-containing fibers leading to samples CB-IRF-400 and CB-IRF-700, respectively (Table 1). The treatment was also done in a tubular furnace at 400 °C for 30 min (sample denoted as H-400). The heating rate was set to 5 °C min⁻¹, and the cooling was done in the furnace overnight, resulting in a slow heat treatment with a total duration of 24 h, including heating and cooling.

The scanning electron micrographs of the samples shown in **Figure 3** demonstrate the evolution of the morphology under different synthesis parameters. The as-spun fibers showed a smooth surface, indicating the presence of the polymer coating. In contrast, the cross-section of the fibers (inset of Figure 3A) showed a grainy texture showing vanadium alkoxide particles. After the heat-treatments of IRF-400 and IRF-700, the formation of VO_x particles can be seen while maintaining the fiber morphology (Figure 3B,C). The smooth surface of as-spun was preserved through heat treatments at 400 °C in H-400 (Figure 3D). This can be due to slower diffusion of oxygen with a lower heating and cooling rate and less burning of the PVA shell. The addition of carbon black is observed by the presence of particles in the fibers, which are maintained without the disintegration of the fiber after heat treatment (Figure 3E–G). Transmission electron micrographs show that the V_2O_3 particles formed during the heat treatment are in the order of a few nanometers and contained in the fiber.

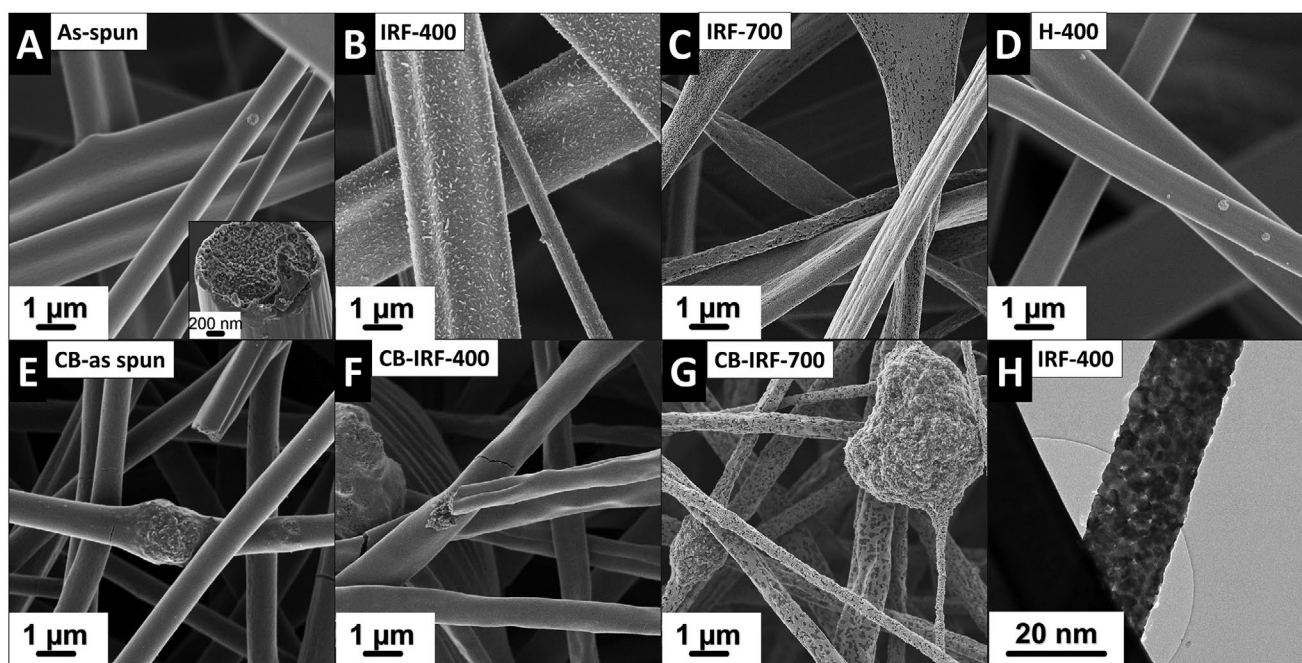


Figure 3. Scanning electron micrographs of A) as-spun VTIP-PVA fibers, inset: cross-section of the fiber. B) H-400, inset: H-400 electrode under bending. C) IRF-400, D) IRF-700, E) as-spun CB-VTIP-PVA, F) CB-IRF-400, G) CB-IRF-700, and H) transmission electron micrograph of IRF-400.

For further morphology analysis, the deviation in the fiber diameter was measured to observe the effect of temperature and heating rate on the diameter of the fibers. For this, 50 points of each sample were measured in the scanning electron micrographs, and their distribution was plotted in Figure 4A. IRF-400 and IRF-700 show a similar fiber diameter distribution with an average of 1.2 ± 0.5 and 1.0 ± 0.5 μm , respectively, while H-400 shows a broader size distribution than the other two with an average of 1.4 ± 0.8 μm . This indicates that the slower heating and cooling rate leads to more heterogeneous fiber diameter distributions. The average diameter of IRF-400 lies below H-400, demonstrating thinner fibers in total, which contribute to sample fragility. IRF-700 shows the lowest average fiber diameter among the three heat-treated fibers.

Homogeneity in the phase was evaluated via X-ray diffraction, and the scans are shown in Figure 4B. For all heat-treated samples, reflections showed a narrow shape and matched the pattern of vanadium trioxide in a rhombohedral lattice, space group $R\bar{3}c$ (167), showing the samples are composed of crystalline V_2O_3 phase. All spectra showed single-phase composition except for the H-400, which presented minor peaks matching other vanadium oxide phases such as VO_2 and V_6O_{11} . The formation of secondary phases can be assigned to the more

prolonged heating and cooling time during the heat treatment, demonstrating higher heterogeneity with slower rates. This duration allows the formation of other oxide phases that are thermodynamically stable at temperatures between room temperature and 400°C but are kinetically less favorable than V_2O_3 in the system.

Raman spectroscopy was additionally performed to observe the bands corresponding to the C–C bonding and their evolution in different samples. The spectra are presented in Figure 4C. The spectrum of the as-spun fibers without carbon shows the main bands at 160 , 266 , 474 , 760 , 890 , and 1012 cm^{-1} , which mostly correspond to vanadium-oxygen bonds. Hardcastle et al. studied the correlation of vanadium-oxygen bond distances and the bond orders,^[28] where the longer interatomic distance between oxygen and vanadium corresponded to lower V–O stretching frequencies. Since the as-spun fiber is made of noncrystalline vanadium oxides and VTIP contains bonds between vanadium and oxygen with different oxidation states,^[29] these multiple bands at different frequencies resemble different V–O bond lengths and its stretching (474 , 760 cm^{-1}), bending (266 cm^{-1}), or external modes (160 cm^{-1}). The broad band shape in the spectrum is indicative of the lack of long-range order in the fibers.^[30] Bands in the spectral region

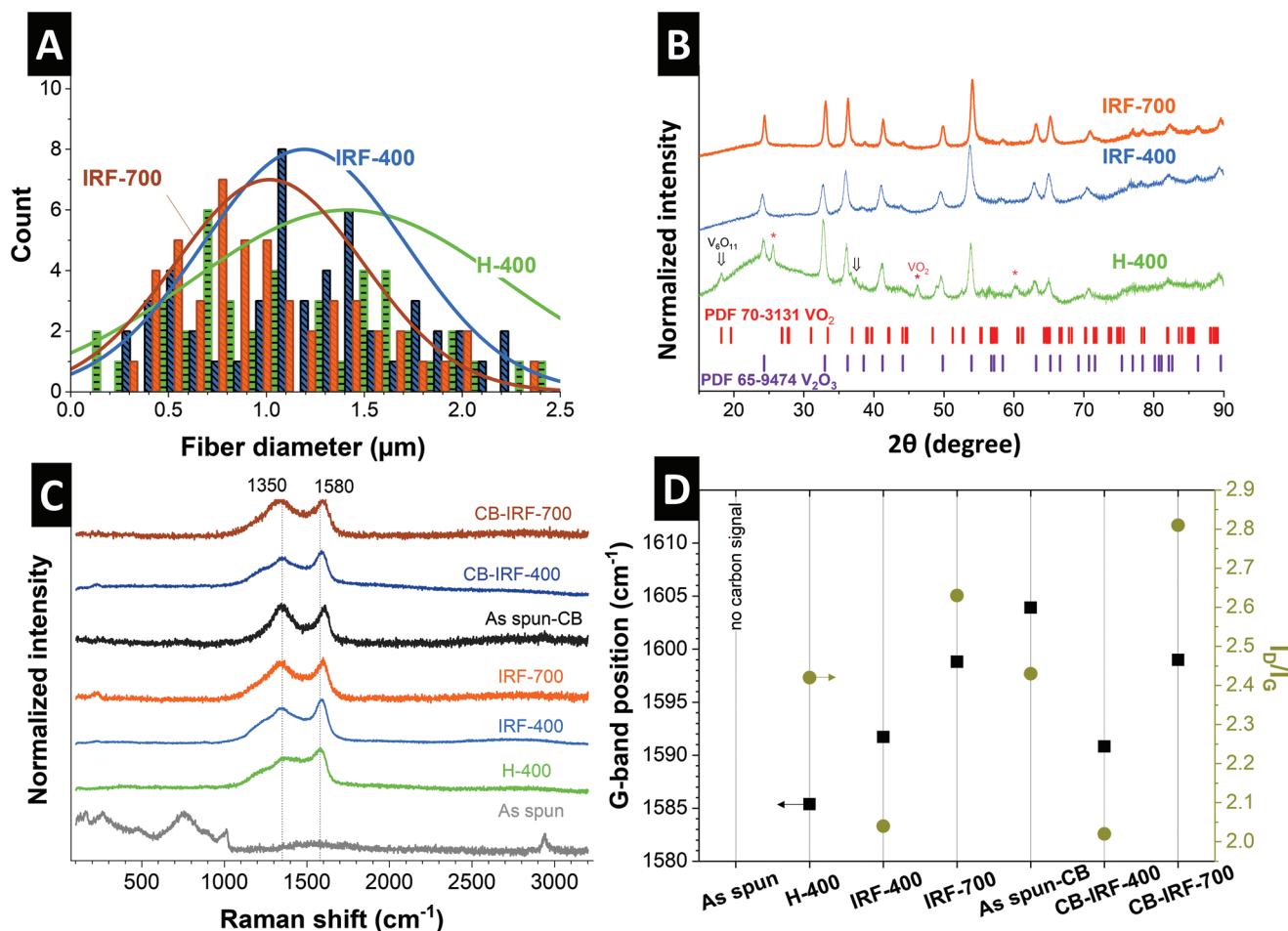


Figure 4. A) Fiber diameter distribution of H-400, IRF-400, and IRF-700. B) X-ray diffractograms of H-400, IRF-400, and IRF-700. C) Raman spectra of as-spun fibers with and without carbon, H-400, IRF-400, IRF-700, CB-IRF-400, and CB-IRF-700, and D) their respective G-band position and I_D/I_G ratio.

of 800–1200 cm^{-1} belong to the vibration of $\text{V}=\text{O}$,^[31] which is present in VTIP. At higher frequencies, a band at $\approx 2940 \text{ cm}^{-1}$ is observed, which is in the CH region^[29] and belongs to the C–H stretching in the CH_3 groups connected to VTIP or the C–H present in the PVA.

All of these bands are hardly distinguished after heat treatment. In all of these samples, C=C and C–C bands belonging to sp^2 -hybridization and sp^3 hybridization were observed as the main present bands (G-band and D-band at 1580 and 1350 cm^{-1} , respectively).^[32] This indicates the presence of conductive carbon in the as-spun fibers due to the carbon black addition and the formation of carbon bonds in the heat-treated samples by removing hydrogen and oxygen atoms in the PVA and forming sp^2 and sp^3 hybridized carbon as a result. The high-frequency band at 2940 cm^{-1} is still observed in the as-spun CB sample due to many C–H bonds but is absent after the heat treatment of PVA. Peak analysis was employed on the D-band and G-band of carbon to investigate the crystallinity and quality of the present carbon in each sample. For this, the G-band position and the ratio of I_D/I_G in different samples calculated from the area under the D-band and G-band are presented in Figure 4D. All samples show a large contribution of the D band and lack of the D-band overtone 2D at 2700 cm^{-1} , indicative of the nanocrystallinity of the carbon in the material. In both carbon-black-containing and parent fibers, the G-band undergoes a blueshift by the heat treatments at 700 °C compared to 400 °C, from 1592 to 1599 cm^{-1} for IRF-400 to IRF-700 and 1591 to 1599 cm^{-1} for CB-IRF-400 to CB-IRF-700, showing more graphitic ordering achieved under higher temperatures. A sharp increase was also observed in I_D/I_G from 2.04 in IRF-400 to 2.63 in IRF-700 and from 2.02 in CB-IRF-400 to 2.81 in CB-IRF-700, which can be due to the coarsening of the vanadium oxide particles and removal of the PVA at a higher temperature, resulting in the defect increase in the carbon shell of the fibers. H-400 showed the lowest G-band position and higher I_D/I_G position than treatments in the infrared furnace. Together, they can imply a lower conductivity of the carbon due to lower graphitization and higher value of defects.

Energy-dispersive X-ray spectroscopy was employed to confirm the presence of oxygen-containing groups and observe the composition change after the heat treatments. Figure 5A shows the elemental analysis for the as-spun and heat-treated samples. All samples show oxygen content of ≈ 22 –33 at%, with carbon-containing samples showing a generally lower amount of oxygen due to the added carbon black. As expected from the synthesis procedure, in the VTIP-CB sample, there is more detected carbon in the fibers than in the VTIP sample. Heat treatments show an increase in vanadium ratio, from 12.6 at% in as-spun fibers to 18.3 at% in H-400, 19.7 at% in IRF-400, and 19.1 at% in IRF-700. Also, in VTIP-CB spun fibers from 10.9 at% to 17.9 at% in CB-IRF-400 and 26.8 at% in CB-IRF-700. Parallel to the vanadium ratio increase in the samples, a general decrease in carbon up to 5 at% is observed. Still, a direct effect of the heat treatment parameters on the elemental composition cannot be concluded. Elemental analysis of the IRF-400 and IRF-700 samples show very similar results, but a different trend is present in the heat-treated samples of VTIP-CB. While in the CB-IRF-400, the carbon ratio stays nearly unchanged and the vanadium ratio increases, in the CB-IRF-700 sample, the carbon percentage decreases drastically. This can indicate the removal of the PVA during the heat treatment. A larger standard deviation for all detected elements also shows less homogeneity caused by PVA removal and particle growth in this sample.

To complement the chemical analysis, thermogravimetric analysis was performed in synthetic air with Ar as the protective gas to calculate the contribution of CB in the carbon content in the fibers after the heat treatment. For this, the samples IRF-400 and CB-IRF-400 were chosen, and their mass change against the temperature is presented in Figure 5B. An initial decrease is observed in both graphs, indicating the fibers' water loss. Following the water loss, a mass increase occurs attributed to the oxidation of V_2O_3 to V_2O_5 . Accompanying this oxidation, a mass decrease starts due to the PVA oxidation and removal. Both V_2O_3 and PVA oxidation end at 400 °C and leave the sample with a plateau at higher temperatures. The difference in the mass of the residues equal to

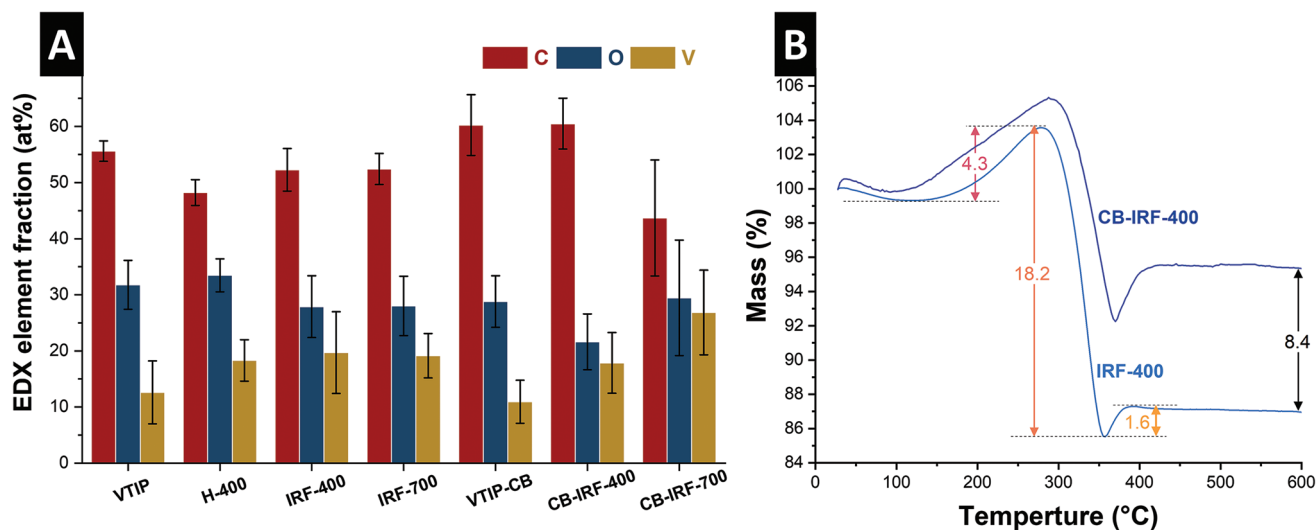


Figure 5. A). Elemental analysis of heat-treated samples by energy-dispersive X-ray spectroscopy. B) Thermogravimetric analysis of IRF-400 and CB-IRF-400 done in synthetic air under 5 °C min^{-1} heating rate.

8.4 mass% indicates the carbon content arising from the CB additive.

3.3. Mechanical Properties of the Fibers

Mechanical stability was examined by cyclic bending of the electrodes to half of their diameter. In contrast to bulk materials, electrospun fibers have low isotropy due to the random, nonwoven fibrous morphology and inhomogeneity in fiber size and direction. Therefore, no standard procedure for examining their mechanical properties has been established. Reports on the mechanical properties of the electrospun fibers can be divided into two groups. One, testing the single fibers via instruments such as AFM and measuring the mechanical properties in the micrometer range,^[14,15] and the other on the macroscopic range and pieces of the electrospun mat.^[14,16] While microscopic measurements can be used for different electrospun fibers and have a higher data precision, they are not scalable to the macroscopic mechanical properties. Additionally, measuring mechanical properties in terms of tensile strength is usually unreproducible when reports on the same materials and conditions are compared.^[22] If the mechanical properties are measured on a microscale, the results vary for different fibers due to the nonwoven nature of the fibers and the difference in size.^[15,33] Therefore, we use macro-bending to analyze the average mechanical behavior under different treatment protocols. The samples were bent to half of their diameter in multiple cycles until crack initiation and subsequent failure (Video S1, Supporting Information). For the fibrous mats, the thickness cannot be directly measured; therefore, samples with similar dimensions (9.5–10 mm) and mass (2.5–3 mg) were chosen to normalize the thickness. No substrate or support, such as polyurethane, was used for the bending to affect the results, and all the samples were bent in their dried state. Different bending rates (mm s^{-1}) were used to observe the sensitivity of the samples to the deformation rate. Each batch tested at least 3 samples to reproduce the results. Despite the samples' anisotropy in fiber morphology, the bending results were similar and in line with the other samples in the same batch.

The samples with an initial defect, such as a crack or a crease, showed a much lower strength and reached failure in the first cycles and could not be compared to samples without initial defects. As-spun fibers were first bent several times under a rate of 1 mm s^{-1} and remained intact for more than 50 cycles. For H-400, the first cracks were observed after 10 cycles of bending to half of the sample diameter, and failure (breaking of the electrode) took place after 50 cycles. H-400 also showed sensitivity to the rate of bending. Under 1 mm s^{-1} , the electrode fractured in the first cycle, while under a bending rate of 0.5 mm s^{-1} , the electrodes withstood 50 cycles before failure. A maximum of 5 mN force was used as the threshold to bend the fibers. The IRF-400 sample showed completely different results compared to H-400. Under the same rate of 0.5 mm s^{-1} , the samples withstood 20 cycles, but all failed before 50 cycles. First cracks were observed earlier than in H-400, namely in the first cycles, before bending 10 times. A maximum of 5 mN was not enough to bend the samples and was increased to 10 mN. This shows higher stiffness of the IRF-samples compared to H-400.

Table 2. Mechanical properties of samples tested via bending.

	Displacement rate [mm s^{-1}]	First cracks [cycle number]	Fracture [cycle number]	Max. compressive load [mN]
As-spun	1	No cracking	No fracture	5
H-400	1	1	<10	5
	0.5	>10	>50	5
IRF-400	0.5	<10	<50	10
CB-IRF-400	0.5	1	<10	50
CB-IRF-700	0.5	Upon assembly	Upon assembly	—

The carbon-containing CB-IRF-400 showed higher brittleness, with early failure after the first cracks. Bending to half the sample diameter was achieved until the maximum force was 50 mN. These failed under 10 cyclic bending, while CB-IRF-700 broke easily when pasting to the testing stage due to extreme brittleness, making further testing impossible. **Table 2** summarizes these results.

The findings show a direct effect of processing parameters on the stability of mechanical flexibility of the fibers under bending. Higher cooling and heating rates and higher temperatures increase the strength of the fibers, which is shown by the maximum needed force to bend the samples while reducing their flexibility. The addition of carbon shows the same trend by hindering the mechanical flexibility of the fibers to undergo bending.

All these observations can be explained by the relation of mechanical performance to the different microstructures of the samples. For comparing the heating and cooling rate, samples H-400 and IRF-400 can be used. The latter, in general, showed higher deformation in the disc, which can be attributed to the thermal strains. Although samples with the least strain were used for bending, the fibers were affected by the thermal stress, and the residual stress in the fibers is probably the reason for the lower resistance of the sample against bending.

The influence of adding carbon can be analyzed by comparing the results of IRF-400 and CB-IRF-400. In the case of CB-IRF-400, the flexibility decreases, but the reason for this brittleness is the extra stress in the fibers due to carbon particles. While the external stress is increased in the fibers due to bending, it creates stress concentration points where there is more inhomogeneity, where the fibers meet the carbon particle in the material, as shown in Figure 3F. Although composed of crystalline V_2O_3 , similar to other samples (Figure S3A, Supporting Information), the brittleness becomes even more severe with a higher treatment temperature that removes the polymer and induces higher thermal stress, as seen for CB-IRF-700.

3.4. Electrochemical Properties of the Fibers

The electrochemical performance of the free-standing fibers was further evaluated. Four samples were chosen to test their performance against lithium chips between 0.01 and 3.5 V versus Li/Li^+ , namely, H-400, IRF-400, CB-IRF-400, and CB-IRF-700.

The cyclic voltammetry of the samples is represented in Figure 6A. The diagram shows very similar voltammograms for all the samples, comprising two peaks in the cathodic sweep at ≈ 1.9 V versus Li/Li⁺ (i) and ≈ 0.8 V versus Li/Li⁺ (ii). These peaks are completed by two oxidation reactions in the anodic sweep at ≈ 1.3 V versus Li/Li⁺ (iii) and ≈ 2.6 V versus Li/Li⁺ (v). An additional anodic peak was observed in the voltammogram of IRF-400 at the potential of ≈ 1.9 V versus Li/Li⁺ (iv). It can be concluded that the lithiation and delithiation mainly occur by two sets of redox peaks at lower and higher potential, as reported in the literature for the V₂O₃ particles.^[24,34–36] Noting the achieved capacity from the rate handling and stability tests and the trend of the capacity change (Figure 6B,C), the predominant lithiation mechanism is through insertion rather than conversion reactions. The galvanostatic charge-discharge profiles (Figure 6D) taken from cycle 150 of the stability test show a similar trend for all sam-

ples, and the lithiation is assumed to take place via insertion in the V₂O₃ lattice by the following reaction^[24,35]



A stability test for 300 cycles in the potential window of 0.01–3.5 V versus Li/Li⁺ was done at a current of 250 mA g⁻¹ (Figure 6B). H-400 showed an initial capacity of 305 mA h g⁻¹, and after a decrease to 280 mA h g⁻¹ in 25 cycles, it stabilized and reached 306 mA h g⁻¹ after 300 cycles. IR-400 showed an initial capacity of 255 mA h g⁻¹ that decreased to 240 mA h g⁻¹ after 15 cycles and showed a similar trend as the H-400. However, the capacity further declined and fell to 216 mA h g⁻¹ after 300 cycles. Its conductive carbon-containing counterpart CB-IRF-400 showed a better performance. Although the initial capacity and decrease were similar to those of IRF-400, the capacity was stabilized at around 250 mA h g⁻¹ for 300 cycles,

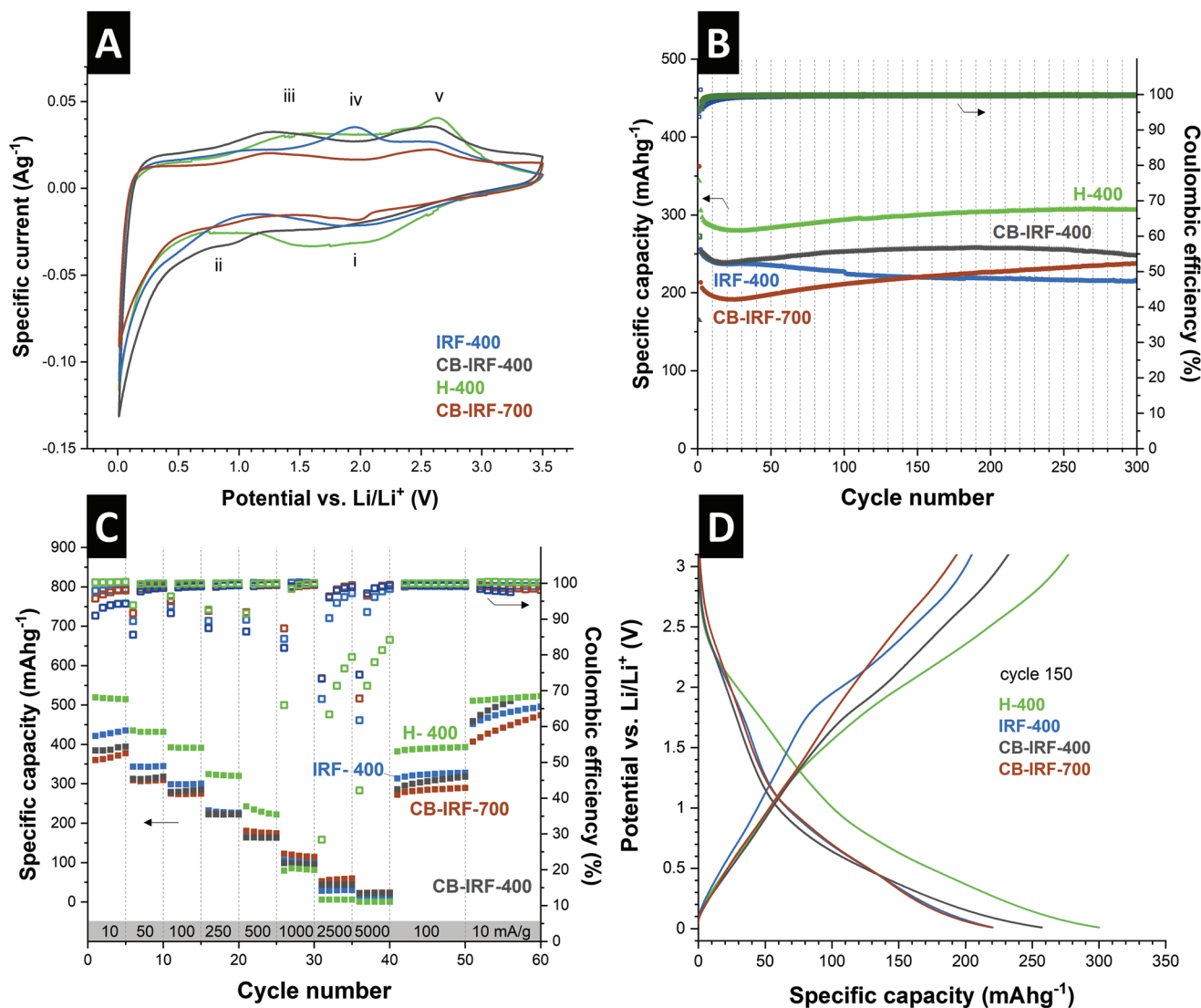


Figure 6. Electrochemical characterization of H-400, IRF-400, CB-IRF-400, and CB-IRF-700 for use as a lithium-ion battery electrode. A) Cyclic voltammograms showing the third cycle at 0.05 mV s⁻¹. B) Stability test at a current rate 250 mA g⁻¹. C) rate handling performance, and D) Galvanostatic charge-discharge curves of the 150th cycle from the stability test at a current rate of 250 mA g⁻¹.

showing a stable performance between H-400 and IRF-400. The CB-IRF-700 sample showed the lowest performance among the four and had an initial capacity of 213 mAh g⁻¹, which decreased to 191 mAh g⁻¹ in 25 cycles and then gradually increased to 238 mAh g⁻¹ after 300 cycles. The H-400 shows the best performance, while CB-IRF-400 and IRF-400 have a lower performance.

This is similar to the results achieved from the mechanical testing of the mats. Since the intactness of the fibers ensures conductive paths for electron movement, it can be deduced that their mechanical stability can directly affect electrochemical performance. This effect can be followed by comparing every two samples in their mechanical and electrochemical performance. The higher cooling rate in the infrared furnace causes more thermal strain on the fibers and makes them more susceptible to breaking. During charging and discharging, the fibers are repeatedly lithiated and delithiated; accordingly, the internal stress from the heat treatment can decrease their ability to buffer the stress from volume change during cycling. As a result, it can be seen that IRF-400 cannot accommodate the capacity of H-400.

Carbon addition makes the fibers more conductive and aids the material with charge transport. This translates into better capacity retention upon long-term cycling, as the carbon ensures conductive pathways even after the mechanical failure of the fibers. Similarly, the presence of carbon enables CB-IRF-400 to outperform IRF-400 at higher rates (Figure 6C). Finally, CB-IRF-700, prepared using a large cooling rate and high-temperature heat treatment, is the most susceptible to breaking, and it shows the lowest performance. Still, the carbon addition in this sample benefits the electrochemical performance, as the comparison with the IRF-700 sample with the same heat treatment but without carbon shows that a lower initial capacity of 121 mAh g⁻¹ is achieved (Figure S3B, Supporting Information).

Therefore, the mechanical properties of the self-standing electrodes can be translated to the electrochemical performance when the chemistry of the samples is the same. For example, when both samples are bare of conductive carbon, electrochemical performance can be directly analyzed by the parameters affecting the brittleness, such as the heat treatment temperature and cooling rate. When the sample's chemical composition is changed by carbon addition, the electrochemical performance enhances, although the carbon addition makes the sample more brittle.

Rate handling was performed at current rates of 10, 50, 100, 250, 500, 1000, 5000 mA g⁻¹ each for 5 cycles and then 10 cycles at rates of 100 and 10 mA g⁻¹ to assess the capacity recovery. All samples went under 5 cycles of conditioning before the rate handling at 10 mA g⁻¹. H-400 showed the highest capacity among the samples, with 520 mAh g⁻¹ at 10 mA g⁻¹ and 390 mAh g⁻¹ at 100 mA g⁻¹. The capacity dropped significantly at higher rates, showing lower conductivity than other samples, as confirmed by Raman analysis (Figure 4C,D). It was again fully recovered and maintained at 100 mAh g⁻¹. The other three samples showed similar rate capability performance with initial capacities of 420, 384, and 360 mAh g⁻¹ for IRF-400, CB-IRF-400, and CB-IRF-700 at 10 mA g⁻¹, respectively. At a higher rate of 2.5 A g⁻¹, CB-IRF-700 retained the highest capacity of 59 mAh g⁻¹, while IRF-400 and CB-IRF-400 showed 30 and

44 mAh g⁻¹, respectively. H-400 lost nearly all of its capacity at 2.5 A g⁻¹. The better performance of carbon-containing samples at a higher rate shows the effect of conductivity and better charge transfer in the fibers. The effect of conductivity can also be observed by the higher Coulombic efficiency in the samples CB-IRF-400 and CB-IRF-700 at higher current rates above 95%, while the Coulombic efficiency for H-400 falls to values below 65% at the highest rates. All samples recovered and maintained their initial capacity at the rate of 10 mA g⁻¹ again, while CB-IRF-400 capacity increased to 520 mAh g⁻¹, close to H-400.

The connectivity of the fibers can explain the observed electrochemical properties. Post mortem scanning electron micrographs of the electrodes after their end of life (Figure S4, Supporting Information) showed the fibers were broken into smaller pieces and lost their initial connection. Since the connectivity of the fibers is the prerequisite for the charge transfer in the material, this elucidates that during cycling, the fiber network loses its connectivity, and through this, its capacity diminishes. Therefore, the parameters mentioned above that affect the capacity can be analyzed through their effect on the connectivity and conductivity of the fibers so that the heat treatment parameter that induces higher thermal stress causes a loss of connectivity in the network and decreases the capacity by isolating the fibers.

4. Conclusions

With the rise of awareness on the sustainability of Li-ion battery electrodes, research has increased in binder-free and NMP-free electrodes. This work aimed to provide a new perspective on preparing flexible electrodes for producing next-generation and more environmentally-friendly electrode materials. We synthesized self-standing vanadium trioxide fibers by electrospinning and subsequent heat treatment. We tested them as Li-ion battery electrodes, showing the relationship between the mechanical and electrochemical performance and how this is affected by processing parameters. We showed that among vanadium oxides, higher oxygen ratios cause fiber brittleness, and particle coarsening. Lower processing temperature was beneficial to the electrode cycling stability. It was observed that lower heating rates affect the performance the most.

Although prolonged heating and cooling induced phase and morphology inhomogeneity, higher mechanical, and electrochemical stability was observed. While in powder materials the synthesis parameters are chosen for the crystallinity and morphology control, in the case of self-standing electrodes, these parameters have to be selected regarding their effect on mechanical flexibility. In the case of faster heating and cooling rates, higher thermal stress is induced in the fibers; therefore, a higher temperature intensifies this effect. This is due to the connection loss between the fibers. More polymer is burned through heat treatments at a higher temperature, and fiber diameter decreases. This can make the fibers more susceptible to breaking under cycling. The same phenomenon occurs when the heat treatment is done with faster heating and cooling rates. This causes the fibers to undergo a greater deformation due to internal thermal stress. Presence of conductive carbon increases the electrochemical stability of the fibers

heat-treated at faster rates by increasing their conductivity, but does not overcome the capacity loss due to the introduced brittleness, as seen by mechanical testing. Therefore, carbon can be added using more mechanically stable species such as CNTs or smaller carbon particles with less aggregation and better dispersion in the sol–gel. Other polymers with higher thermal stability can also improve mechanical properties. PVA has small monomer molecules with –OH functional group per two carbon atoms removed during the heat treatment. This is rather a large mass loss that triggers deformation in the fibers and results in the burning of the carbon atom. Polymers with other monomers and less functional groups can increase flexibility by reducing the diameter and shape loss in the heat treatment and will be used in future works.

Supporting Information

Supporting Information is available from the Wiley Online Library or from the author.

Acknowledgements

This work was part of the electrospun vanadium oxide and sulfide-carbon hybrids project (HEROES-4-Li-NA-batteries) by the German Research Foundation (DFG, Deutsche Forschungsgemeinschaft), Project No. 452180147. The authors thank Zhihao Tien for help with bending tests, Xuan Zhang for useful discussions, and Eduard Arzt (all at INM) for his continuing support.

Open access funding enabled and organized by Projekt DEAL.

Conflict of Interest

The authors declare no conflict of interest.

Author Contributions

B.B.: Conceptualization, Methodology, Investigation, Data curation, Validation, Writing—Original Draft, Writing—Review and Editing. M.G.: Validation, Writing—Review and Editing. S.H.: Methodology, Validation, Supervision, Visualization, Writing—Review and Editing. V.P.: Methodology, Validation, Supervision, Funding Acquisition, Visualization, Writing—Review and Editing.

Data Availability Statement

The data that support the findings of this study are available from the corresponding author upon reasonable request.

Keywords

binder-free electrodes, electrospinning, energy storages, flexible electrodes, vanadium oxide

Received: August 27, 2022

Revised: November 14, 2022

Published online: December 5, 2022

- [1] L. Persano, A. Camposeo, C. Tekmen, D. Pisignano, *Macromol. Mater. Eng.* **2013**, 298, 504.
- [2] D. H. Reneker, I. Chun, *Nanotechnology* **1996**, 7, 216.
- [3] R. Gopal, S. Kaur, Z. Ma, C. Chan, S. Ramakrishna, T. Matsuura, *J. Membr. Sci.* **2006**, 281, 581.
- [4] T. Okuda, K. Tominaga, S. Kidoaki, *J. Controlled Release* **2010**, 143, 258.
- [5] Y. Hong, X. Chen, X. Jing, H. Fan, B. Guo, Z. Gu, X. Zhang, *Adv. Mater.* **2010**, 22, 754.
- [6] M. Ikegame, K. Tajima, T. Aida, *Angew. Chem., Int. Ed. Eng.* **2003**, 42, 2154.
- [7] R. Sahay, P. S. Kumar, R. Sridhar, J. Sundaramurthy, J. Venugopal, S. G. Mhaisalkar, S. Ramakrishna, *J. Mater. Chem. B* **2012**, 22, 12953.
- [8] V. Aravindan, J. Sundaramurthy, P. S. Kumar, Y.-S. Lee, S. Ramakrishna, S. Madhavi, *Sci. Rev. Chem. Commun.* **2015**, 51, 2225.
- [9] M. J. Laudenslager, R. H. Scheffler, W. M. Sigmund, *Pure Appl. Chem.* **2010**, 82, 2137.
- [10] S. He, W. Chen, *Nanoscale* **2015**, 7, 6957.
- [11] Y. Kang, C. Deng, Y. Chen, X. Liu, Z. Liang, T. Li, Q. Hu, Y. Zhao, *Nanoscale Res. Lett.* **2020**, 15, 112.
- [12] D. Chen, Z. Lou, K. Jiang, G. Shen, *Adv. Funct. Mater.* **2018**, 28, 1805596.
- [13] C. Lu, W.-w. Liu, H. Li, B. K. Tay, *Sci. Rev. Chem. Commun.* **2014**, 50, 3338.
- [14] F. Croisier, A. S. Duwez, C. Jerome, A. F. Leonard, K. O. van der Werf, P. J. Dijkstra, M. L. Bennink, *Acta Biomater.* **2012**, 8, 218.
- [15] S. Y. Gu, Q. L. Wu, J. Ren, G. J. Vancso, *Macromol. Rapid Commun.* **2005**, 26, 716.
- [16] Y. Ding, P. Zhang, Z. Long, Y. Jiang, F. Xu, W. Di, *J. Membr. Sci.* **2009**, 329, 56.
- [17] C. F. Armer, J. S. Yeoh, X. Li, A. Lowe, *J. Power Sources* **2018**, 395, 414.
- [18] A. Tolosa, S. Fleischmann, I. Grobelsek, V. Presser, *ACS Appl. Energy Mater.* **2018**, 1, 3790.
- [19] Y. L. Cheah, N. Gupta, S. S. Pramana, V. Aravindan, G. Wee, M. Srinivasan, *J. Power Sources* **2011**, 196, 6465.
- [20] L. Mai, L. Xu, C. Han, X. Xu, Y. Luo, S. Zhao, Y. Zhao, *Nano Lett.* **2010**, 10, 4750.
- [21] C. Ban, N. A. Chernova, M. S. Whittingham, *Electrochem. Commun.* **2009**, 11, 522.
- [22] T. U. Rashid, R. E. Gorga, W. E. Krause, *Adv. Eng. Mater.* **2021**, 23, 2100153.
- [23] S. Y. Chew, T. C. Hufnagel, C. T. Lim, K. W. Leong, *Nanotechnology* **2006**, 17, 3880.
- [24] T. Zhang, L. Zhang, L. Zhao, X. Huang, W. Li, T. Li, T. Shen, S. Sun, Y. Hou, *Small* **2020**, 16, 2005302.
- [25] T. Jin, H. Li, Y. Li, L. Jiao, J. Chen, *Nano Energy* **2018**, 50, 462.
- [26] C. Capello, U. Fischer, K. Hungerbühler, *Trends Green Chem.* **2007**, 9, 927.
- [27] Z. Song, S. W. Chiang, X. Chu, H. Du, J. Li, L. Gan, C. Xu, Y. Yao, Y. He, B. Li, *J. Appl. Polym. Sci.* **2018**, 135, 45787.
- [28] F. D. Hardcastle, I. E. Wachs, *J. Phys. Chem. C: Nanomater. Interfaces* **1991**, 95, 5031.
- [29] J.-C. Panitz, A. Wokaun, *J. Phys. Chem. C: Nanomater. Interfaces* **1996**, 100, 18357.
- [30] P. Shvets, O. Dikaya, K. Maksimova, A. Goikhman, *J. Raman Spectrosc.* **2019**, 50, 1226.
- [31] S.-H. Lee, H. M. Cheong, M. J. Seong, P. Liu, C. E. Tracy, A. Mascarenhas, J. R. Pitts, S. K. Deb, *Solid State Ionics* **2003**, 165, 111.
- [32] A. C. Ferrari, J. Robertson, *Phys. Rev. B* **2000**, 61, 14095.
- [33] L. M. Bellan, J. Kameoka, H. G. Craighead, *Nanotechnology* **2005**, 16, 1095.
- [34] X. Liu, R. Liu, L. Zeng, X. Huang, X. Chen, C. Zheng, Y. Xu, Q. Qian, M. Wei, Q. Chen, *New J. Chem.* **2017**, 41, 5380.
- [35] Y. Sun, S. Jiang, W. Bi, C. Wu, Y. Xie, *J. Power Sources* **2011**, 196, 8644.
- [36] Y. Dong, R. Ma, M. Hu, H. Cheng, J.-M. Lee, Y. Y. Li, J. A. Zapien, *J. Power Sources* **2014**, 261, 184.